

Simulation and optimisation of terahertz emission from InGaAs and InP photoconductive switches

J. Lloyd-Hughes,* E. Castro-Camus, and M.B. Johnston
*University of Oxford, Department of Physics, Clarendon Laboratory,
 Parks Road, Oxford, OX1 3PU, United Kingdom*
 (Dated: Uploaded to arxiv: 11th July 2005)

We simulate the terahertz emission from laterally biased InGaAs and InP using a three-dimensional carrier dynamics model in order to optimise the semiconductor material. Incident pump pulse parameters of current Ti:Sapphire and Er:fiber lasers are chosen, and the simulation models the semiconductor's bandstructure using parabolic Γ , L and X valleys, and heavy holes. A greater total emitted terahertz power is observed as the InGaAs alloy approaches InAs, and is attributed to an increased electron mobility. Additionally, low-temperature grown and ion-implanted InGaAs are modelled using a finite carrier trapping time. At sub-picosecond trapping times the terahertz bandwidth is found to increase significantly at the cost of a reduced emission power. Finally, we find that the simulation results are only weakly affected over the experimentally measured range of intervalley deformation potential.

PACS numbers: 42.72.Ai, 73.20.Mf, 78.20.Bh, 78.47.+p

I. INTRODUCTION

The ability to create and detect single cycle pulses of coherent terahertz (THz) radiation has enabled diverse studies in condensed matter physics. Recent examples include a study of how surface plasmon polaritons propagate on semiconductor gratings,¹ determining the low-energy vibrational modes of oligomers,² and measuring the time-dependent intersubband absorption in semiconductor quantum wells.³ Such studies have become possible because of the development of high power, broadband THz radiation emitters based on photoconductive switches.⁴ Single cycle THz pulses can be generated using ultra-short (~ 10 fs) pulses of above bandgap energy, light incident on a photoconductive switch. Photoexcited electrons and holes are accelerated in opposite directions by an electric field applied between two metallic contacts. By a time of the order of 100 fs after the arrival of the exciting pulse the carriers have screened the applied electric field,⁵ following which momentum scattering decreases the net current flow. This transient rise and fall in current produces a single cycle pulse of electromagnetic radiation, with a broad spectrum in the far-infrared. Experimentally, THz pulses from low-temperature (LT-) grown GaAs photoconductive switches can have spectra covering the frequency range from 0.1 THz to above 30 THz (wavelength range 3 mm to 10 μ m).⁶

While GaAs-based photoconductive switch technology is well developed, the use of a low bandgap semiconductor ($E_F < 0.8$ eV) would enable cheaper, more stable, turnkey THz spectroscopy setups based on erbium fiber (Er:fiber) lasers, which can produce pulses as short as 65 fs at a central wavelength $\lambda = 1.55$ μ m.⁷ Combining a compact system of this type with communications wavelength optical fibres would enable THz pulses to be generated and detected in small, extreme, or otherwise inaccessible environments (e.g. in an endoscope or in the cavity of a pulsed magnet). A suitable low bandgap semi-

conductor is the ternary alloy $\text{In}_{1-x}\text{Ga}_x\text{As}$, in which the range $0.35 \leq E_F \leq 1.42$ eV can be accessed by varying the alloy fraction x.

A few experimental studies have demonstrated THz emission from InGaAs photoconductive switches. Baker *et. al.*⁸ reported a THz imaging system based on a 16 μ m gap bow-tie photoconductive switch emitter, with a ± 50 V ac bias at 22 kHz. Carriers in the switch were excited by 120 fs pulses from a 1.06 μ m Nd glass laser, and the semiconductor was LT-In_{0.3}Ga_{0.7}As with a 550 fs carrier trapping time. THz power was observed up to ~ 3 THz. Additionally, Suzuki and Tonouchi⁹ have measured the THz emission from photoconductive switches made from In_{0.53}Ga_{0.47}As implanted by 340 keV, 1×10^{15} cm⁻² Fe ions. They used an Er:fiber laser with central wavelength 1.56 μ m and pulse duration 300 fs, and measured THz power up to ~ 2 THz. Finally, Mangeney *et. al.*¹⁰ performed a similar experiment on In_{0.53}Ga_{0.47}As implanted by Au⁺ ions, with a carrier lifetime of 0.9 ps.

In order to investigate suitable semiconductors for photoconductive switch THz emitters it is beneficial to adopt a modelling approach. The effect of altering one parameter (or more) of the semiconductor material or laser can be investigated rapidly, and an optimum combination sought. While analytical models of THz emission are relatively straightforward to interpret, they often require phenomenological assumptions (e.g. about carrier mobilities). In this paper we therefore employ a three-dimensional semi-classical carrier dynamics simulation, which has been used previously to model the THz emission from InAs and GaAs surfaces under a magnetic field,¹¹ ion-implanted GaAs surfaces¹² and GaAs photoconductive switches.⁵ After detailing the laser and semiconductor parameters used in Sec. II, we report on the simulated THz emission from $\text{In}_{1-x}\text{Ga}_x\text{As}$ photoconductive switches in Sec. III. In Sec. III A we discuss how propagation through the semiconductor alters the emit-

ted THz radiation, using the TO phonon-polariton dielectric function. A comparison between E_{THz} from the binary III-V semiconductors InAs, GaAs and InP is made in Sec. III B. During Secs. III C, III D and III E we investigate how the carrier trapping time, choice of alloy fraction and incident pulse energy alter the emitted THz power and bandwidth. Finally, how the experimental uncertainty in the values of the intervalley deformation potential and surface pinning potential may affect these results is discussed in Sec. III F.

II. SIMULATION DETAILS

The carrier dynamics model used herein is an extension of that described in Refs. 5,11,12. A set of 10^6 pseudoparticles comprising extrinsic and photogenerated carriers and fixed ions are used to simulate the semiconductor. At each 5 fs step in time the model numerically finds the three-dimensional potential due to the charge density, subject to the appropriate boundary conditions for the surface and Schottky photoconductive switch contacts. Carrier-carrier, carrier-phonon and carrier-impurity scattering mechanisms are included.¹¹ The simulated particles are within a box of size $x \times y \times z = 6 \times 6 \times 4 \mu\text{m}^3$, subdivided into a grid of $64 \times 64 \times 32$, as shown in Fig. 1(a). The contacts of the photoconductive switch are at $-3 \leq x \leq -1 \mu\text{m}$ and $1 \leq x \leq 3 \mu\text{m}$. A constant bias voltage of 5 V between electrodes was used throughout this work, which corresponds to typical experimental field strengths E . The simulation starts at a time $t = -0.7 \text{ ps}$, to allow the extrinsic carriers to equilibrate before the arrival of the incident pulse (Fig. 1(b)), which has peak intensity at time $t = 0.0 \text{ ps}$, and is centred at $x, y = 0$.

A. Properties of InGaAs

While a property of a ternary alloy cannot be obtained simply from a linear interpolation between the value for its constituent binary compounds, this is a useful first approximation, particularly when experimental data is limited. A more accurate value may be obtained using a bowing parameter B that accounts for the deviation from linearity. For example, the direct band gap energy of $\text{In}_{1-x}\text{Ga}_x\text{As}$ may be written as a function of alloy fraction x as:

$$E_{\Gamma}(x) = (1 - x)E_{\Gamma}^{\text{InAs}} + xE_{\Gamma}^{\text{GaAs}} - x(1 - x)B_{E_{\Gamma}} \quad (1)$$

where the bowing parameter $B_{E_{\Gamma}} = 0.477 \text{ eV}$ is assumed independent of temperature,¹³ and E_{Γ} denotes the band gap energies of InAs and GaAs. Values of semiconductor parameters for $\text{In}_{1-x}\text{Ga}_x\text{As}$ were generated automatically within the simulation using the bowing parameter if available in the literature, or by linear interpolation if not. The parameters required in the simulation are

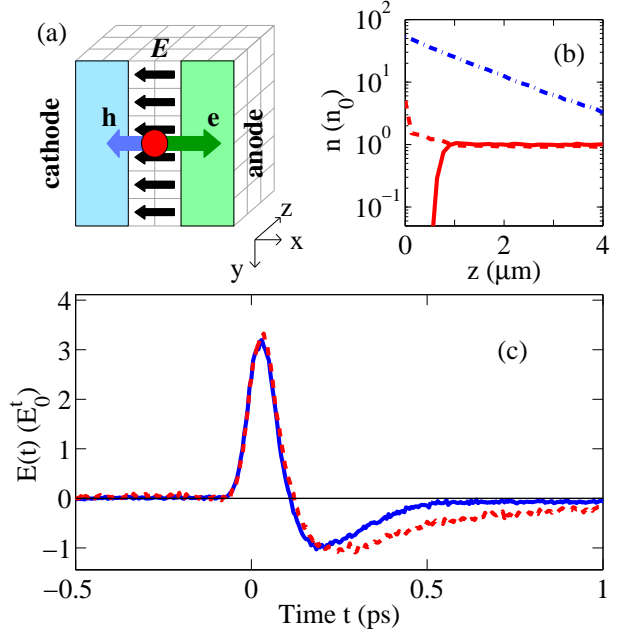


FIG. 1: (Color online) (a) Geometry of the box and grid used in the simulation (see text). (b) Electron density n in model for $\text{In}_{0.53}\text{Ga}_{0.47}\text{As}$ (n -type doping density $1 \times 10^{15} \text{ cm}^{-3}$) as a function of depth z from surface, at $x = 0$ and averaged over y direction. n is in units of $n_0 = 1 \times 10^{15} \text{ cm}^{-3}$. At $t = -0.25 \text{ ps}$ the simulated extrinsic electrons are in equilibrium: when the surface pinning potential $V_{\text{pin}} = -0.5E_{\Gamma}$ (defined in Sec. III F), a depletion region close to the surface ($z = 0$) can be seen (solid line), while with $V_{\text{pin}} = +0.5E_{\Gamma}$, there is an electron accumulation region (dashed line). Also plotted is the electron density (dash-dotted line) at $t = 0.00 \text{ ps}$, dominated by photoexcited electrons. (c) Simulated E_{THz} calculated from $E_{\text{THz}} \propto \partial J_x / \partial t$ for n-type $\text{In}_{0.53}\text{Ga}_{0.47}\text{As}$ with $V_{\text{pin}} = -0.5E_{\Gamma}$ (solid line) and $V_{\text{pin}} = +0.5E_{\Gamma}$ (dashed line), where J_x is the current density in the x direction averaged over the entire box.

listed in Table I for $\text{In}_{0.53}\text{Ga}_{0.47}\text{As}$, together with values for GaAs, InAs and InP.

Although the simulation assumes a parabolic band structure for simplicity, in the modelling of THz emission from narrow band-gap semiconductor surfaces the inclusion of the L-valley was found to create a more realistic carrier energy distribution.¹¹ In photoconductive switches the average carrier energy is greater than for surface emitters, and intervalley (e.g. $\Gamma \rightleftharpoons L$) scattering by absorption or emission of an optical phonon becomes more significant. Further, in the range $0.4 \lesssim x \lesssim 0.7$ the X-valley energy gap of $\text{In}_{1-x}\text{Ga}_x\text{As}$ falls below that of the L-valley. The simulation was therefore extended to include the X valley in addition to the Γ and L valleys.

The inspection of the properties of InGaAs suggests that it may have advantages and disadvantages as a THz emitter compared with GaAs. Firstly, a higher electron mobility (due primarily to a lower effective mass) should result in greater THz power. Secondly, the intervalley deformation potential $D_{\Gamma-L}$ is greater for InAs than GaAs,

TABLE I: Parameters used in the simulation (at room temperature and pressure), from Refs. 13,14. For InGaAs, values of the bowing parameter B for each property are in brackets, taken from Ref. 13. When no bowing parameter was found in the literature, linear interpolation between InAs and GaAs was used and the value is given in *italic*. The two-mode TO phonon energies for InGaAs were taken from Ref. 16. For consistency the intervalley deformation potential D_{ij} was taken from Ref. 15, the only reference found with values for GaAs, InAs and InP.

Parameter	GaAs	In _{0.53} Ga _{0.47} As	InAs	InP
Γ valley band-gap energy E_Γ (eV)	1.42	0.73 (0.477)	0.354	1.34
L valley offset $E_{L-\Gamma}$ (eV)	0.29	0.58 (0.33)	0.73	0.59
X valley offset $E_{X-\Gamma}$ (eV)	0.48	0.56 (1.4)	1.02	0.85
Γ valley effective mass (m_Γ^*)	0.067	0.039 (0.0091)	0.022	0.08
L valley effective mass (m_L^*)	0.56	<i>0.41</i>	0.29	0.63
X valley effective mass (m_X^*)	0.85	<i>0.73</i>	0.64	0.66
Heavy hole effective mass (m_{hh}^*)	0.5	0.45 (-0.145)	0.40	0.60
Number of valleys $\beta_\Gamma, \beta_L, \beta_X$	1, 4, 3	1, 4, 3	1, 4, 3	1, 4, 3
LO phonon energy (meV)	36.0	<i>33.0</i>	30.0	43.0
TO phonon energy (meV)	33.5	<i>31.6, 28.3</i>	26.7	38.1
$D_{\Gamma L}$ (eV/m)	0.4×10^{10}	<i>0.7×10^{10}</i>	1.0×10^{10}	1.8×10^{10}
$D_{\Gamma X}$ (eV/m)	2.9×10^{10}	<i>2.5×10^{10}</i>	2.2×10^{10}	2.6×10^{10}
Acoustic phonon deformation potential (eV)	7.0	<i>5.9</i>	5.0	6.0
Speed of sound (ms ⁻¹)	5240	<i>4693</i>	4280	5080
Mass density ρ (kg m ⁻³)	5360	<i>5506</i>	5667	4810
Static/high frequency dielectric constant $\epsilon_s, \epsilon_\infty$	12.95, 10.89	13.9 (0.67), 11.6	15.15, 12.25	12.5, 9.61
Absorption coefficient α (μm^{-1}) [$\lambda = 800\text{nm}$]	1.2	0.8 [$\lambda = 1.55\mu\text{m}$]	6.5	2.5

resulting in a larger intervalley scattering rate. When electrons scatter to the L or X valley they lose kinetic energy, contributing to the deceleration of carriers that produces the negative peak in E_{THz} . The lower absorption coefficient (α) of InGaAs at $1.55\mu\text{m}$ compared with GaAs at 800 nm is a disadvantage, because a lower α results in a lower bandwidth for defect-laden semiconductors, owing to the photogeneration of fewer carriers within the damaged depth. In addition, with a smaller α the emitted THz radiation will on average travel further through the semiconductor (when the reflection geometry⁶ is used), and will be more significantly affected by absorption and dispersion.

Finally, since $\text{In}_{1-x}\text{Ga}_x\text{As}$ exhibits two-mode TO phonon behaviour¹⁶ the THz spectra will exhibit strong absorption peaks near the TO phonon energies (e.g. for $x=0.47$ the two modes have frequencies of 6.8 and 7.6 THz). This will limit the spectroscopic use of $\text{In}_{1-x}\text{Ga}_x\text{As}$ photoconductive emitters in the frequency range near and between the TO phonon modes of InAs and GaAs (6.4 and 8.1 THz). It should be noted that the intervalley and LO phonon scattering mechanisms included in the simulation assume single-mode behaviour. However, the effect that two-mode TO phonons have on THz emission from a photoconductive switch can be modelled via the TO phonon-polariton dielectric function, as described in Sec. III A.

B. Laser parameters

The simulation uses incident pulse parameters characteristic of current ultra-short mode-locked lasers (i.e. a Gaussian spatial and temporal shape, and a transform-limited Gaussian energy distribution). For the case of a 10 fs Ti:sapphire laser (with central wavelength $\lambda = 800\text{nm}$, $\Delta\lambda = 80\text{nm}$, typical beam power $P_{\text{exp}} = 400\text{mW}$ and a repetition rate $R = 75\text{MHz}$) we use a simulation power of $10\mu\text{W}$ and a Gaussian spot of standard deviation $\sigma_{x,y} = 0.5\mu\text{m}$ in order to obtain the same photon flux as experimentally achievable. While amplified Er:fiber lasers have been demonstrated with pulse durations of 65 fs ($\lambda = 1550\text{nm}$, $\Delta\lambda > 100\text{nm}$, $P_{\text{exp}} = 110\text{mW}$, $R = 67\text{MHz}$),⁷ sub-30 fs pulses widely tunable over the wavelength range 1130 to 1950 nm may be generated by coupling such Er:fiber laser light into a highly non-linear fiber.¹⁷ For excitation around $1.55\mu\text{m}$ we use $P = 6\mu\text{W}$ and $\sigma_{x,y} = 0.5\mu\text{m}$, chosen to give the same photon flux as for the Ti:sapphire, so that a comparison between In_{0.53}Ga_{0.47}As switches excited by $1.55\mu\text{m}$ radiation, and GaAs excited by 800 nm can be made in Section III B. With the aim of providing a quick reference to the laser parameters used we refer below to the 10 fs, $\lambda = 800\text{nm}$ Ti:sapphire just described as laser A, and the 65 fs $\lambda = 1.55\mu\text{m}$ Er:fiber as laser B.

III. RESULTS

The simulated THz emission from $\text{In}_{1-x}\text{Ga}_x\text{As}$ photoconductive switches is presented in this section, initially via qualitative discussion and comparison with simulations for InP and GaAs (Sec. III B). By including the effect of carrier-trapping defects we then simulate E_{THz} for low-temperature or ion-implanted $\text{In}_{1-x}\text{Ga}_x\text{As}$ (Sec. III C). Subsequently, we investigate in Sec. III D how the choice of alloy fraction x impacts THz emission efficiency for excitation pulses of 65 fs duration, and $\lambda = 1.55 \mu\text{m}$.

In order to enable a comparison between the results presented below we normalize E_{THz} in the time and frequency domains to the peak simulated values for a GaAs photoconductive switch excited by laser A (with carrier trapping time $\tau_c = 100 \text{ ps}$), denoted E_0^t and E_0^v respectively. Similarly the emitted THz power (defined as the square of $E_{\text{THz}}(t)$ integrated over all times) is normalized to P_0 , the power for the GaAs emitter.

A. THz propagation through photoconductive switch

In the far-field the THz electric field E_{THz} radiated by a large-aperture photoconductive switch is related to the current density \mathbf{J} by:

$$\mathbf{E}_{\text{THz}} \propto \frac{1}{1 + \sqrt{\epsilon}} \frac{\partial \mathbf{J}}{\partial t} \quad (2)$$

where the dielectric function ϵ is in general complex, and frequency dependent.¹⁸ We use this relation to calculate E_{THz} from our simulation, modelling ϵ using the well-known Drude dielectric function for TO phonon-polaritons,¹⁹ which for two TO phonon modes is given by:

$$\epsilon_{\text{TO}}(\omega, x) = \epsilon_{\infty}^x + \frac{\epsilon_s^x - \epsilon_s^{x=1}}{1 - \omega^2/\omega_{x=0}^2 - i\omega\Gamma/\omega_{x=0}^2} + \frac{\epsilon_s^{x=1} - \epsilon_{\infty}^x}{1 - \omega^2/\omega_{x=1}^2 - i\omega\Gamma/\omega_{x=1}^2} \quad (3)$$

where ϵ_s^x , ϵ_{∞}^x are the low and high frequency dielectric constants at alloy fraction x . The angular frequency of the GaAs-like (InAs-like) TO phonon is $\omega_{x=1}$ ($\omega_{x=0}$). The damping rate is assumed to be $\Gamma = 0.06 \text{ ps}^{-1}$ for both InAs-like and GaAs-like TO phonon modes.¹⁹ In Fig. 2(a) the refractive index n and absorption coefficient α for $\text{In}_{0.53}\text{Ga}_{0.47}\text{As}$ are given. In order to estimate the thickness of semiconductor through which the emitted THz must propagate we plot in Fig. 2(b) the maximum THz electric field (calculated from Eqn. 2) from each ‘slice’ parallel to the surface. As expected from the photoexcited carrier density (Fig. 1(b)), E_{THz} mainly originates from close ($z < 1 \mu\text{m}$) to the surface. Taking the mean of this distribution results in a weighted propagation thickness of $\sim 0.5 \mu\text{m}$. If the emitted THz radiation from a photoconductive switch is collected in the reflection geometry absorption and dispersion in the semiconductor material can be minimized⁶. Therefore $0.5 \mu\text{m}$ is a reasonable estimate of the propagation distance of THz radiation in an InGaAs photoconductive switch.

In Fig. 2(c) the spectrum of the simulated E_{THz} from an $\text{In}_{0.53}\text{Ga}_{0.47}\text{As}$ photoconductive switch (Fig. 1(c)) is shown, as calculated using Eqn. 2 ignoring the term containing ϵ (solid line). If the THz radiation is instead calculated using Eqn. 2 with ϵ from Eqn. 3, and is assumed to propagate through $0.5 \mu\text{m}$ of semiconductor and into free space, then the dotted line of Fig. 2(c) results. The spectral amplitude of transmitted THz radiation clearly reduces close to the TO phonon frequencies,

and is enhanced just above the LO phonon frequencies (7.25 THz, 7.95 THz) because of a larger transmission coefficient when n is small.²⁰ It is important not to misinterpret these spectral peaks as arising from the emission of THz radiation from LO phonons, which cannot in general couple to propagating electromagnetic fields. In the time-domain (Fig. 2(c) inset), the transmitted E_{THz} exhibits damped oscillations due to the two TO phonon modes, but at a higher frequency $\omega_{\text{T+}}$ corresponding to the minimum of the upper TO phonon-polariton branch.²¹ We apply the propagation model just described in generating all the results presented below.

B. Semiconductor choice

Historically, the choice of semiconductor material in broadband THz emitters based on photoconductive switches has been limited by the wavelength of ultra-short mode-locked lasers, because of the necessity of above bandgap energy radiation in creating a photoexcited carrier population. Typically therefore GaAs (room temperature bandgap $E_{\Gamma} = 1.42 \text{ eV}$) and $\lambda = 800 \text{ nm}$ (energy $E_{\gamma} = 1.55 \text{ eV}$) Ti:Sapphire lasers are used.⁶ While InP ($E_{\Gamma} = 1.34 \text{ eV}$) is also a suitable material for 800 nm excitation, there only a few studies in the literature.^{22,23}

In Fig. 3 we compare the simulated E_{THz} for InP and GaAs excited by 10 fs pulses from laser A with that obtained for InAs excited by 65 fs pulses from laser B. These

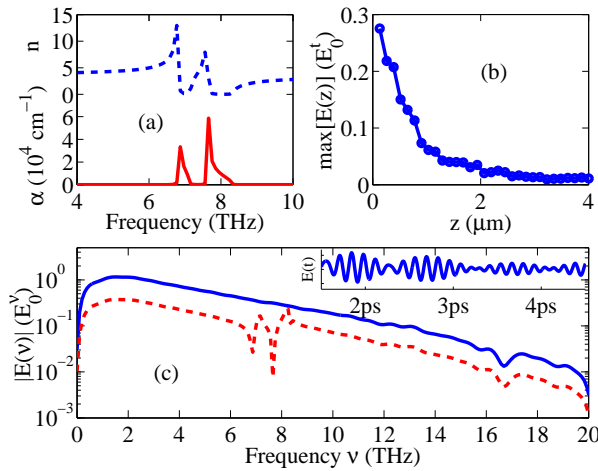


FIG. 2: (Color online) (a) Refractive index n (dotted line) and absorption coefficient α (dashed) calculated from the two TO phonon Drude model form (Eqn. 3) for $\text{In}_{0.53}\text{Ga}_{0.47}\text{As}$. The InAs-like and GaAs-like TO phonon frequencies are $\omega_{x=0}/2\pi = 6.8 \text{ THz}$ and $\omega_{x=1}/2\pi = 7.6 \text{ THz}$. (b) Maximum value of E_{THz} when calculated for each simulation ‘slice’ in the plane parallel to the semiconductor surface, as a function of depth z from the surface. (c) Effect of propagation on simulated spectra. Spectra of simulated E_{THz} for $\text{In}_{0.53}\text{Ga}_{0.47}\text{As}$ (solid line) from Fig. 1(c) ($\tau_c = 0.3 \text{ ps}$, laser B parameters). When Eqn. 2 is used, and E_{THz} is propagated through $0.5 \mu\text{m}$ of $\text{In}_{0.53}\text{Ga}_{0.47}\text{As}$ and into free space the spectrum (dashed line) exhibits characteristic local minima close to the TO phonon frequencies, and local maxima close to the LO-phonon frequencies. (Inset) Damped, beating oscillations are observed in the time-domain.

parameters were chosen to enable a comparison between THz systems based on current state-of-the-art lasers. The peak value of E_{THz} for InAs is larger than for GaAs, despite the Er:fiber laser’s power being lower than that of the Ti:sapphire (the photon flux is the same for both lasers). This can be attributed in part to a higher fraction of incident photons having above bandgap energy. As the inset of Fig. 3 indicates, almost 100% of photons from laser B have energy greater than $E_{\Gamma}(\text{InAs}) = 0.35 \text{ eV}$, while the above bandgap fraction for laser A is smaller ($\sim 80\%$). The fact that InAs has a lower Γ valley electron effective mass than GaAs also contributes to the power increase. Qualitatively, a smaller effective mass produces a larger mobility $\mu = e\tau/m^*$, which should result in a larger transient current and therefore power. However, this argument neglects changes in the carrier scattering time τ , and we return to this point in Sec. III E.

Turning now to E_{THz} for InP, we observe a slightly greater peak time domain and spectral amplitude than for GaAs, despite the larger m_{Γ}^* (lower mobility) of InP. This is again related to the energy distribution of the incident infrared pulses. Defining the excess energy of the incident pulse as $\Delta = E_{\gamma} - E_{\Gamma}$ we see that $\Delta = 0.21 \text{ eV}$ for InP, while $\Delta = 0.13 \text{ eV}$ for GaAs. A greater percentage of incident photons are therefore absorbed in

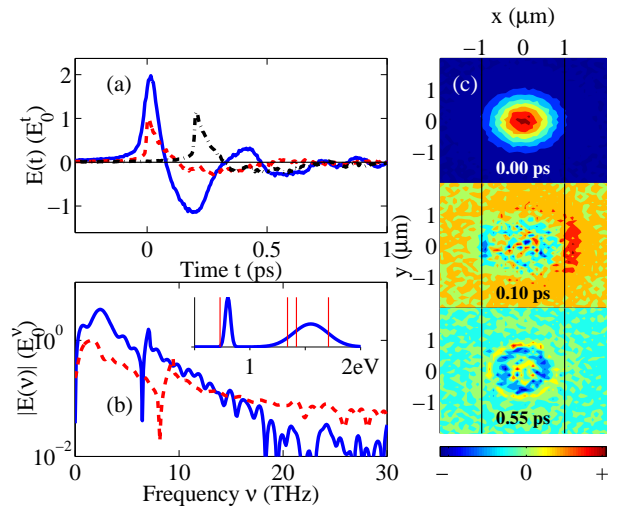


FIG. 3: (Color online) (a) Simulated E_{THz} for GaAs (dashed line) and InP (dash-dotted line, offset in time by $+0.2 \text{ ps}$ for clarity) photoconductive switches excited by laser A, and InAs (solid line) excited by laser B. Both InP and InAs have a larger peak E_{THz} than GaAs. (b) Fourier transform of $E_{\text{THz}}(t)$ from (a), for InAs (solid) and GaAs (dashed line). The spectrum for InP (not shown) is substantially the same as that for GaAs (with its TO phonon absorption at 9.2 THz). (Inset) Schematic energy distributions of a transform-limited 65 fs pulse at $\lambda = 1.55 \mu\text{m}$ (0.8 eV) and a 10 fs pulse at $\lambda = 800 \text{ nm}$ (1.55 eV). Vertical lines at 0.73 eV , 1.34 eV , 1.42 eV and 1.71 eV respectively indicate E_{Γ} for $\text{In}_{0.53}\text{Ga}_{0.47}\text{As}$, InP and GaAs, and E_L for GaAs. (c) Change in electron density between simulation time steps in the plane of the surface ($x - y$), averaged over the depth z (see text for discussion). The black lines at $x = -1 \mu\text{m}$ and $x = 1 \mu\text{m}$ mark the positions of the cathode and anode.

InP ($\sim 91\%$) than GaAs (80%), contributing to a larger E_{THz} .

The simulated E_{THz} for InAs exhibits an extra oscillatory component after $t = 0.30 \text{ ps}$, due to the onset of charge-density oscillations that can radiate THz radiation. These plasma-type oscillations can be observed directly in the simulation as a change in electron density between time steps (Fig. 3(c)). At $t = 0.00 \text{ ps}$ the rapid increase in electron density is due to photoexcitation, and produces the first positive peak in E_{THz} . By $t = 0.10 \text{ ps}$ there is an increased electron density at the anode, while the first negative peak in E_{THz} is at $t = 0.2 \text{ ps}$ (Fig. 3(a)), and is primarily a result of the rapid momentum scattering of electrons. The subsequent change in E_{THz} for $t > 0.3 \text{ ps}$ can be identified as resulting from circular regions of altering charge density (Fig. 3(c), $t = 0.55 \text{ ps}$). Plasma oscillations have been observed previously in the simulation of THz emission from InAs surfaces,¹¹ and become less noticeable as $x \rightarrow 1$ due to GaAs’s lower mobility.

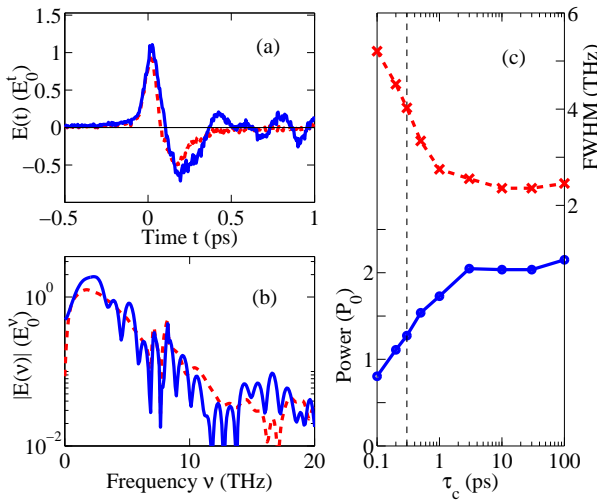


FIG. 4: (Color online) (a) Simulated E_{THz} for $\text{In}_{0.53}\text{Ga}_{0.47}\text{As}$ with $\tau_c = 100$ ps (solid line) and $\tau_c = 0.3$ ps (dashed line), using 65 fs pulses with laser B's parameters. (b) Fourier transform of (a). In (c) the power (circles) and FWHM (crosses) are plotted for $\tau_c = 0.1 - 100$ ps, showing a significant reduction in power and a bandwidth increase as τ_c decreases below 1 ps. The power is normalized to that of GaAs with $\tau_c = 100$ ps (excited by laser A), P_0 . The dotted vertical line indicates $\tau_c = 0.3$ ps, used in subsequent figures.

C. Carrier trapping time

Higher bandwidth terahertz emission can be achieved by introducing defects into a semiconductor using a technique such as high energy ion-implantation, or low-temperature (LT) semiconductor growth. In both cases, carriers are trapped on sub-picosecond time scales, with carrier trapping times τ_c as short as 550 fs in LT-In_{0.3}Ga_{0.7}As (Ref. 8) and 300 fs in In_{0.53}Ga_{0.47}As implanted with 2 MeV Fe ions.²⁴ When τ_c becomes comparable with the duration of a single-cycle THz pulse ($\tau_c \lesssim 1$ ps) bandwidth improvements can be observed. This effect may be modelled using an exponential reduction in the photoexcited carrier density,¹² with a time constant τ_c .

In Fig. 4 we present the simulated THz electric field E_{THz} and calculated spectra for In_{0.53}Ga_{0.47}As excited by 65 fs pulses of 1.55 μm centre wavelength light, as a function of carrier trapping time. At shorter values of τ_c the negative peak in E_{THz} arrives earlier, creating an increase in the spectral full-width-at-half-maximum (FWHM). This trend can be seen in Fig. 4(c): when $\tau_c \lesssim 1$ ps there is a rapid increase in FWHM at the cost of a reduced power, where power is defined as $E_{\text{THz}}^2(t)$ summed over all simulation times.

In the following sections we choose an experimentally achievable value of $\tau_c = 0.3$ ps.

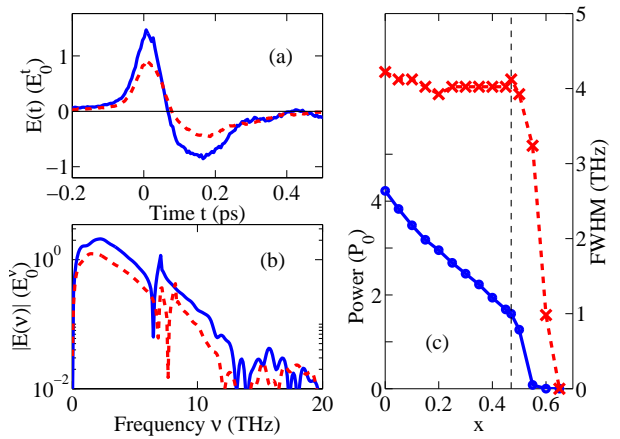


FIG. 5: (Color online) (a) and (b) Simulated E_{THz} for InAs (solid lines) and In_{0.53}Ga_{0.47}As (dashed lines) with $\tau_c = 0.3$ ps and excited by 65 fs, $\lambda = 1.55\mu\text{m}$ pulses from laser B. (c) Power (circles) and FWHM (crosses) as of simulated E_{THz} as a function of x . The dotted vertical line indicates $x = 0.47$.

D. Effect of varying Ga alloy fraction at $\lambda = 1.55\mu\text{m}$

With the intention of optimizing the semiconductor for excitation at 1.55 μm we modelled the THz emission from In_{1-x}Ga_xAs at alloy fractions x in the range $0 \leq x \leq 0.7$. The results of this set of simulations are shown in Fig. 5. The emitted power increases towards InAs to over five times larger than that of GaAs excited by laser A, while the FWHM remains constant. When $x \gtrsim 0.45$ both the power and FWHM drop dramatically, since the excess incident pulse energy Δ becomes small and then negative, and fewer photoexcited carriers are created.

While these results should be relatively straightforward to verify experimentally, the density and kinetic energy of photoexcited carriers alter significantly when x is varied and λ kept constant. To try to assess better how the material choice alters THz emission (independent of the laser's parameters) we performed a further set of simulations at constant excess excitation energy Δ , as reported in the next section.

E. Effect of varying Ga alloy fraction at constant excess pulse energy Δ

Simulations were run over the full range of alloy fraction x with constant $\Delta = 0.07$ eV and photoexcited carrier density. Pulsed Er:fiber lasers widely tunable in the range 1130 to 1950 nm (1.1 to 0.64 eV) have been recently developed,¹⁷ which should allow experimental studies of this kind over a significant range of alloy fraction ($0.37 \lesssim x \lesssim 0.77$).

As Fig. 6(a) shows, the emitted THz power increases towards $x=0$, as found in Sec. IIID. By extracting the carrier momentum scattering time τ from the simulation (averaged over all electrons in the Γ valley, and taken

at $t = 0.00$ ps) we estimate the electron mobility $\mu(x) \simeq e\tau(x)/m_\Gamma^*(x)$. As can be seen in Fig. 6(b), the relative increase in $\mu(x)$ towards InAs compares favourably with the experimental low-field mobility for $\text{In}_{1-x}\text{Ga}_x\text{As}$.

Shortly after the peak incident pulse intensity the electric field applied across a photoconductive switch is completely screened by the build-up of the THz-emitting dipole. This occurs in a characteristic screening time $t_s \sim 100$ fs for a semi-insulating GaAs photoconductive switch.⁵ By calculating the electric field at the incident spot position ($x, y = 0$ μm) as a function of time, it is possible to extract the screening time t_s , defined as the time at which the electric field becomes zero. Figure 6(b) indicates that t_s increases as the Ga alloy fraction $x \rightarrow 1$, as a result of the lower electron mobility. It should be noted that a shorter screening time does not necessarily mean a reduction in the THz power emitted: a higher mobility can produce both a lower t_s and a greater power.

This simulation set was repeated for incident pulse durations of 10 fs and 100 fs. In the 10 fs case the total power emitted (Fig. 6(a)) is smaller than for 65 fs across the entire range of x , as fewer carriers are photoexcited. However, for 100 fs the power is again lower than the 65 fs case, because when the later carriers are photoexcited the electric field is already partly screened. How the THz power and bandwidth alter as a function of incident pulse duration was discussed for semi-insulating GaAs in Ref. 5. The FWHM of the 100 fs spectra are lower than those of the 10 fs and 65 fs simulations, owing to the slow rise in E_{THz} . Somewhat counterintuitively, the 10 fs spectra do not have greater FWHM than the 65 fs over the whole range of x . This can be explained by noting that the FWHM measures the width of the spectrum, and not the high-frequency spectral tail. Thus while greater spectral amplitude is obtained at high frequencies for 10 fs excitation (e.g. Fig. 3(b)), the amplitude at low-frequency (which dominates the FWHM) is larger at incident pulse durations of 65 fs.

F. Experimentally uncertain parameters

A few semiconductor parameters that are less well known experimentally could influence the trends reported here. One of these is the intervalley deformation potential D_{ij} , the characteristic strength of intervalley electron-phonon scattering, in which an electron absorbs or emits a near zone-edge phonon and transfers to another valley. The momentum scattering rate $W_{ij}(k)$ used in the simulation has been derived by e.g. Refs 25,26, and is:

$$W_{ij}(k) = \frac{\pi\beta_j D_{ij}^2}{\omega_j \rho} N(E_{\mathbf{k}} \pm \hbar\omega_j - E_{j-i}) \left(f_B(\hbar\omega_j) + \frac{1}{2} \mp \frac{1}{2} \right) \quad (4)$$

where i and j represent the initial and final valleys (e.g. Γ and L), $E_{\mathbf{k}}$ is the electron's kinetic energy above the val-

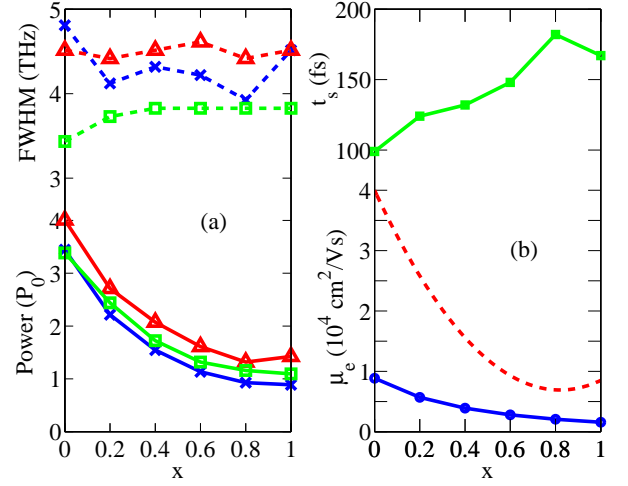


FIG. 6: (Color online) (a) Power (solid lines) and FWHM (dashed lines) of simulated THz electric field from $\text{In}_{1-x}\text{Ga}_x\text{As}$ ($\tau_c = 0.3$ ps.), for incident pulse durations of 10 fs (crosses), 65 fs (triangles), and 100 fs (squares). The photon energy above the bandgap and the incident photon density were kept constant as the alloy fraction x was varied. (b) The average Γ valley electron mobility (solid line) extracted from the simulation (see text for description), can be compared with the (low carrier energy) Hall mobility (dashed line). The time t_s in which the applied electric field becomes screened (squares) increases towards GaAs.

ley's minimum, and $f_B(\hbar\omega_j)$ is the Bose-Einstein distribution function. ω_j is the angular frequency of zone-edge phonons, where it has been assumed in the derivation of Eqn. 4 that TO and LO phonon modes have the same (wavevector independent) frequency. The density of final electron states is N , and the other symbols are as defined in Table I.

There is a considerable range in the values of D_{ij} reported in the literature, even for well characterized semiconductors such as GaAs. For GaAs the reported values of $D_{\Gamma-L}$ range from 0.4×10^{10} eVm⁻¹ (theoretically found, using a rigid ion pseudopotential method,¹⁵ to 1×10^{11} eVm⁻¹ (measured using the Gunn effect), and 7×10^{10} eVm⁻¹ (using non-equilibrium phonon spectroscopy).^{27,28}

So as to assess how this uncertainty may affect our simulation results, we plot in Fig. 7 the simulated E_{THz} for GaAs excited by laser A as a function of $D_{\Gamma-L}$. As $D_{\Gamma-L}$ increases the THz pulse shortens (and the emitted THz power decreases) because of the higher $\Gamma - L$ scattering rate. The increase in $D_{\Gamma-L}$ from 0.4×10^{10} eVm⁻¹ to 1.0×10^{10} eVm⁻¹ from GaAs to InAs therefore counteracts the overall rise in power towards $x=0$ seen in Figs. 5 and 6. Even if $D_{\Gamma-L}$ happened to vary between 0.4×10^{10} eVm⁻¹ and 2.0×10^{11} eVm⁻¹ from $x=1$ to $x=0$, Fig. 7 suggests that the power drop due to increased intervalley electron-phonon scattering would not counterbalance the rise in power.

The FWHM are approximately constant for $D_{\Gamma-L} \geq$

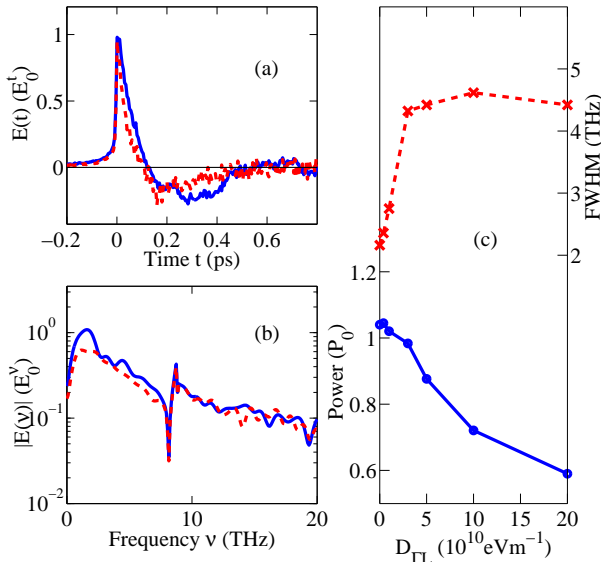


FIG. 7: (Color online) Simulated THz electric field from GaAs as a function of intervalley deformation potential $D_{\Gamma L}$. (a) Simulated E_{THz} for $D_{\Gamma L} = 0$ (solid line) and $D_{\Gamma L} = 2.0 \times 10^{11} \text{ eVm}^{-1}$ (dashed line), and (b) shows the Fourier transform of (a). In (c) the power (circles) and FWHM (crosses) for simulations run as a function of $D_{\Gamma L}$ are given. Laser parameters A (10 fs Ti:Sapphire) were used.

$3 \times 10^{10} \text{ eVm}^{-1}$, and while there is a noticeable decrease in FWHM below this value (because of the appearance of the spectral peak near 2 THz, associated with plasma oscillations) the spectral shape does not dramatically change.

A second parameter that is not known accurately is the value of the surface field pinning potential for InGaAs. At a semiconductor surface singly occupied atomic orbitals (dangling bonds) create surface states that pin the Fermi level at an energy V_{pin} , and these states create an electric field near the surface. A change in V_{pin} cannot directly alter the THz emission from a photoconductive switch, since dipoles formed by charges separating under a surface field cannot radiate in the direction perpendicular to the surface (the x or y directions). However, a different surface field could arguably alter the charge carrier distribution, which via interactions between the hot and cold carriers might thereby affecting THz emission.

Difficulties in ensuring clean, oxide-free surfaces make the accurate measurement of V_{pin} challenging. In GaAs $V_{\text{pin}} \simeq -0.5E_\Gamma = -0.7 \text{ eV}$ (relative to the Γ valley minimum), and there is an electron depletion field near the surface. In contrast, for InAs $V_{\text{pin}} \simeq 0.1 \text{ eV}$ (i.e. at the surface the conduction band is below the Fermi level), and an electron accumulation region forms.²⁹ Accordingly, we varied the pinning potential in the range $-0.5 \leq V_{\text{pin}}/E_\Gamma \leq 0.5$ for $\text{In}_{1-x}\text{Ga}_x\text{As}$, and found a small change in the simulated E_{THz} . In Fig. 1(b) the depletion (accumulation) region formed when $V_{\text{pin}} = -0.5E_\Gamma$ ($V_{\text{pin}} = +0.5E_\Gamma$) for $\text{In}_{0.53}\text{Ga}_{0.47}\text{As}$ is shown, and Fig. 1(c) shows the corresponding simulated E_{THz} for $\tau_c = 0.3 \text{ ps}$.

When $V_{\text{pin}} < 0$ (i.e. depletion region) the emitted THz pulse is slightly shorter in duration than when $V_{\text{pin}} > 0$ (accumulation region). The spectra (not shown) are substantially the same, except for a reduction in spectral power at low frequency ($< 1 \text{ THz}$) for the shorter duration pulse. The mean scattering rate of electrons in the Γ valley was found to be lower for $V_{\text{pin}} > 0$, due to a reduction in the electron-hole scattering rate W_{e-h} . This can be attributed to a higher electron density near the surface for an accumulation field, since $W_{e-h} \sim 1/n$.^{25,26} The power when $V_{\text{pin}} = +0.5E_\Gamma$ was found to be $\sim 1.2 \times$ the power at $V_{\text{pin}} = -0.5E_\Gamma$, i.e. as the $\text{In}_{1-x}\text{Ga}_x\text{As}$ alloy approaches InAs the power enhancement should be slightly increased by the presence of an accumulation region near the surface.

IV. CONCLUSION

In summary, we have simulated the terahertz emission from $\text{In}_{1-x}\text{Ga}_x\text{As}$ photoconductive switches over the entire alloy fraction range $0 \leq x \leq 1$. Two methods for increasing the THz power from photoconductive switches were identified. Firstly, a larger electron mobility resulted in a larger THz power as the Ga alloy fraction was decreased. This suggests that semiconductors with high mobility/low effective mass may be used to improve THz power, for example InAs ($m_\Gamma^* = 0.022m_e$) or InSb ($m_\Gamma^* = 0.014m_e$). Experimentally, a high resistivity or semi-insulating InAs may be required to produce a photoconductive switch with a low dark current. Secondly, increased THz power can be obtained by judicious choice of incident pulse energy, so that the majority of photons are absorbed.

The spectra calculated from the simulation indicate that InAs photoconductive switches have greater power than GaAs over the frequency range $0 - 15 \text{ THz}$. At higher frequencies, the initial rise in E_{THz} (dominated by the incident pulse duration) governs the amplitude. This result seems to suggest that an InAs/65 fs Er:fiber laser setup should produce THz pulses that are at least as powerful as those from 10 fs Ti:sapphire/GaAs setups.

Additionally, we have investigated the significance of a few parameters that are less well known. The variation due to uncertainty in the intervalley deformation potential was not found to produce an effect large enough to counteract the results here. Changing the pinning potential to create an electron accumulation region rather than a depletion region was observed to increase the low frequency THz power.

V. ACKNOWLEDGEMENTS

The authors would like to thank the EPSRC, the Royal Society (UK) and CONACyT (México) for financial support.

-
- ^{*} Electronic address: james.lloyd-hughes@physics.ox.ac.uk
- ¹ J. G. Rivas, M. Kuttge, P. H. Bolivar, H. Kurz, and J. A. Sanchez-Gil, Phys. Rev. Lett. **93**, 256804 (2004).
- ² M. B. Johnston, L. M. Herz, A. L. T. Khan, A. Köhler, A. G. Davies, and E. H. Linfield, Chem. Phys. Lett. **377**, 256 (2003).
- ³ T. Muller, W. Parz, G. Strasser, and K. Unterrainer, Phys. Rev. B **70**, 155324 (pages 5) (2004).
- ⁴ P. Smith, D. Auston, and M. Nuss, IEEE J. Quantum Electron. **24**, 255 (1988).
- ⁵ E. Castro-Camus, J. Lloyd-Hughes, and M. B. Johnston, Phys. Rev. B **71** (2005).
- ⁶ Y. C. Shen, P. C. Upadhyay, E. H. Linfield, H. E. Beere, and A. G. Davies, Appl. Phys. Lett. **83**, 3117 (2003).
- ⁷ F. Tauser, A. Leitenstorfer, and W. Zinth, Opt. Expr. **11**, 594 (2003).
- ⁸ C. Baker, I. S. Gregory, W. R. Tribe, I. V. Bradley, M. J. Evans, M. Withers, P. F. Taday, V. P. Wallace, E. H. Linfield, A. G. Davies, et al., Appl. Phys. Lett. **83**, 4113 (2003).
- ⁹ M. Suzuki and M. Tonouchi, Appl. Phys. Lett. **86**, 051104 (2005).
- ¹⁰ J. Mangeney, L. Joulaud, P. Crozat, J.-M. Lourtioz, and J. Decobert, Appl. Phys. Lett. **83**, 5551 (2003).
- ¹¹ M. B. Johnston, D. M. Whittaker, A. Corchia, A. G. Davies, and E. H. Linfield, Phys. Rev. B **65**, 165301 (2002).
- ¹² J. Lloyd-Hughes, E. Castro-Camus, M. D. Fraser, C. Jagadish, and M. B. Johnston, Phys. Rev. B **70**, 235330 (2004).
- ¹³ I. Vurgaftman, J. R. Meyer, and L. R. Ram-Mohan, Journal of Applied Physics **89**, 5815 (2001).
- ¹⁴ *NSM semiconductor archive*, URL <http://www.ioffe.rssi.ru/SVA/NSM/Semicond/>.
- ¹⁵ S. Zollner, S. Gopalan, and M. Cardona, J. Appl. Phys. **68**, 1682 (1990).
- ¹⁶ J. Groenen, R. Carles, G. Landa, C. Guerret-Piecourt, C. Fontaine, and M. Gendry, Phys. Rev. B **58**, 10452 (1998).
- ¹⁷ F. Tauser, F. Adler, and A. Leitenstorfer, Opt. Lett. **29**, 516 (2004).
- ¹⁸ J. Shan and T. F. Heinz, *Ultrafast Dynamical Processes in Semiconductors* (Springer-Verlag Berlin Heidelberg, 2004), chap. 1, pp. 1–56.
- ¹⁹ P. Y. Yu and M. Cardona, *Fundamentals of Semiconductors* (Springer, 2003), 3rd ed.
- ²⁰ A. Leitenstorfer, S. Hunsche, J. Shah, M. C. Nuss, and W. H. Knox, Phys. Rev. Lett. **82**, 5140 (1999).
- ²¹ For the case of zero damping and at zero phonon wavevector $\omega_{T+} = \omega_{LO}$, which is why the LO phonon frequency can enter the mathematical description of a TO phonon-polariton without being physically involved.
- ²² P. K. Benicewicz and A. J. Taylor, Opt. Lett. **18**, 1332 (1993).
- ²³ T. Hattori, S. Arai, and K. Tukamoto, Jpn. J. Appl. Phys. Part 1 **43**, 7546 (2004).
- ²⁴ C. Carmody, H. H. Tan, C. Jagadish, A. Gaarder, and S. Marcinkevicius, Appl. Phys. Lett. **82**, 3913 (2003).
- ²⁵ *Numerical Simulation of Submicron Semiconductor Devices* (Artech House Inc., Boston, 1993), chap. 2.5.
- ²⁶ B. K. Ridley, *Quantum Processes in Semiconductors* (Clarendon Press, Oxford, 1999), chap. 4.3.
- ²⁷ C. L. Collins and P. Y. Yu, Phys. Rev. B **30**, 4501 (1984).
- ²⁸ D.-S. Kim and P. Y. Yu, Phys. Rev. B **43**, 4158 (1991).
- ²⁹ S. Ono, M. Takeuchi, and T. Takahasi, Appl. Phys. Lett. **78**, 1086 (2001).